WILEY-VCH

DOI: 10.1002/ ((please add manuscript number))

Fast Photoresponse from 1T Tin Diselenide Atomic Layers

Peng Yu,† Xuechao Yu,† Wanglin Lu,† Di Wu, Hsin Lin, Linfeng Sun, Kezhao Du, Fucai Liu, Wei Fu, Qingsheng Zeng, Zexiang Shen, Chuanhong Jin, Qi Jie Wang, and Zheng Liu,**

P. Yu, K. Du, F. Liu, W. Fu, Q. Zeng, Prof. Z. Liu
School of Materials Science and Engineering
Nanyang Technological University
50 Nanyang Avenue, Singapore 639798, Singapore
X. Yu, Prof. Q. J. Wang
School of Electrical and Electronic Engineering
Nanyang Technological University
50 Nanyang Avenue, Singapore 639798, Singapore
W. Lu, Prof, C. H. Jin
State Key Laboratory of Silicon Materials
School of Materials Science & Engineering
Zhejiang University
Hangzhou, Zhejiang, 310027, P. R. China
L. Sun, Prof. Z. X. Shen
School of Physical and Mathematical Sciences
Nanyang Technological University, 639798, Singapore
D. Wu, Prof. H. Lin
Department of Physics
National University of Singapore, 117542, Singapore
†These authors contributed equally to this work.

1. Introduction

Stimulated by the discovery of graphene and its fascinating electronic and physical properties,[1-4] two-dimensional (2D) materials such as hexagonal boron nitride (h-BN),[5-8] transitional metal chalcogenides (TMDs)[9-15] and other 2D compounds,[16-18] have received increasing interests because of their great potential in the field of catalysis, nanotribology, microelectronics, lithium batteries, hydrogen storage, medical and optoelectronics.[19-22] However, their applications in nanoelectronic and optoelectronic devices are limited by the zero bandgap of graphene. The high leaking current in graphene based field-effect transistor (FET) make it difficult for realization of integrated circuits. For 2D compounds in a form of MX_2 (M = transitional and main group metal, X = S, Se and Te), it typically crystallizes in 2H and 1T types structure with D_{6h} and D_{3d} point-group symmetry respectively and the major difference between 2H and 1T is the coordination type of the metal atoms: the trigonal prismatic coordination for the former and the octahedral coordination, in addition, “2” and “1” in 2H and 1T represent the number of the layers in unit cell, shown in Figure S1. Substantial

efforts have been devoted to study 2H type MX_2 2D crystals (e.g. MoS_2, WSe_2), because of their stable phase. Potential applications such as valleytronics, ultra-low-power consumption electronics and high performance catalyst were reported. For example, FETs fabricated using TMD MX_2 (M = Mo and W, X = S and Se) atomic layers exhibit excellent on/off current ratio (up to 10^8) and reasonably good carrier mobility,[22], [23] and some MX_2 (M = Nb and Ta, X = S and Se) thin films show exciting superconductivity and charge density wave (CDW) behaviors.[22], [24], [25]

However, it shed less light on the electronic and optoelectronic properties of 1T-MX_2 2D crystals simply due to the difficulties in synthesis. In addition, the metallic nature of some 1T phase 2D layers make them not suitable to the fabrications of FET and optoelectronic devices (such as, M = Mo, W, Nb and Ta, X = S, Se and Te).[26] 1T-MX_2 2D crystals, however, show several advantages compared with their 2H phase counterparts, e.g., 1T monolayer WS_2 displays the better electrocatalytic and photocatalytic properties.[27], [28] Therefore, the research of electronic and optoelectronic properties of atomically thin layers of 1T MX_2 2D materials is highly demanding.

Among 1T MX_2 2D crystals, $SnSe_2$ is a semiconductor with bulk band gap of about 1.0 eV. For a thick $SnSe_2$ film (84 nm) based device, it showed a mobility of 28 $cm^2V^{-1}s^{-1}$ but a poor on/off ratio in single digit, and a high bulk electron affinity of 5.2 eV according to recent report.[29] In addition, $SnSe_2$ films is also a good candidate for resistive memory and solar cells.[30] However, most of the studies currently focused on thick or bulk $SnSe_2$.[29], [31] The properties of atomic layered $SnSe_2$ are still unknown.

In this paper, mono-layered and bi-layered $SnSe_2$ are firstly successfully exfoliated via mechanical exfoliation from the single-crystal $SnSe_2$, which have been carefully examined their electronic and optoelectronic behaviors. Complementary characterizing tools such as atomic force microscope (AFM) and Raman microscopy have been employed to characterize the $SnSe_2$ atomic layers. The optoelectronic properties of the bilayer $SnSe_2$ devices were systematically studied, which show a mobility of ~ 4 $cm^2V^{-1}s^{-1}$ and on/off ~ 10^3. More interestingly, atomic layered $SnSe_2$ exhibits high photoresponsivity reaching 0.5 AW^{-1} and very fast response speed of 2.2 ± 0.3 ms (rise) and 3.2 ± 0.2 ms (fall), exceeding most of other 2D materials like MoS_2 and WSe_2 layers. These make few-layer $SnSe_2$ a promising active 2D material for electronic and optoelectronic applications.

2. Result and Disccusion

2.1. Synthesis and crystal structure of of $SnSe_2$ single crystals

$SnSe_2$ crystallizes with a hexagonal space group $P\text{-}3m_1$ of the CdI_2-type, which consists of the $SnSe_6$ octahedral layers bonded together by weak van der Waal's forces to form 1T structure but an anisotropic atomic structure shown in Figure 1a. The single crystals SnSe2 bulk with the definite metallic sheen shown in Figure 1c have been synthesized by the direct transport method without the transport gas (Figure 1b and S2), which have been confirmed by the powder X-ray diffraction (XRD) (Figure S3) and the energy dispersive X-ray spectroscope (EDX) with the formula of $SnSe_{1.96(2)}$ (Figure 1d), consistent with the calculation formula $SnSe_2$. The atomic structure of our $SnSe_2$ is also confirmed by the atomically resolved annual dark-field (ADF) scanning transmission electron microscopy (STEM), as shown in Figure 2 and S4. $SnSe_2$ flakes have been mechanically exfoliated from bulk single crystals onto the SiO_2/Si (285 nm thick SiO_2) substrate using the scotch tape, and then transferred to TEM grids. Figure 2a displayed the film dominated by bi-layered $SnSe_2$. Inset is the Fast Fourier Transform (FFT) pattern which shows six-fold-symmetric spots, indicating the hexagonal structure of the samples. Monolayer $SnSe_2$ can be also observed at some locations, which is indicated by a white rectangle in Figure 2a. This same region is presented in Figure 2b, where we can clearly identify the sites of Sn and In atoms. The Sn–Sn bond length is estimated to be ~ 0.37 nm. This value fits to the simulation and model very well in Figure 2c and 2d.

2.2. AFM and Raman spectra of atomically thick $SnSe_2$ flakes

Figure 3a shows monolayer $SnSe_2$ with lateral dimensions exceeding 13 μm. Similar to other 2D atomic layers, the thickness of $SnSe_2$ layer can be roughly determined via the contrast of its optical images. In order to identify exactly the number of layers, AFM images are obtained from dashed-line region in Figure 3a. From the AFM images shown in Figure 3c, monolayer $SnSe_2$ is found along the edge with a thickness of ~ 0.87 nm. It is slightly more than the actual thickness of 0.62 nm (Figure 1a) likely due to the trapping of absorbed molecular (e.g., H_2O) between the flake and the substrate and the measuring error of AFM, similar to the thickness variations in monolayer SnS_2 (1.0 ± 0.2 nm VS 0.6 nm).[32] In addition, the thickness of 2L, 3L, 4L and 5L $SnSe_2$ are 1.48, 2.13, 2.69 and 3.36 nm shown in Figure S5, respectively, which are also lightly more than the theoretical values, 1.24, 1.86, 2.48 and 3.1 nm. Therefore, the distances between 1L and 2L, 2L and 3L, 4L and 5L are 0.61, 0.65, 0.56 and 0.67 nm, which is basically in accordance with the thickness of monolayer, 0.67 nm.

Raman spectroscopy is a powerful nondestructive characterization tool to confirm the phase of 2D crystals. The Raman spectrum of bulk 1T $SnSe_2$ has been reported by the previous papers, indicated that there were two vibratory modes E_g (in-plane vibration) and A_{1g} (out-plane

vibration) with the values of 116.0 and 185.5 cm^{-1} in 300 K excited by the 488 nm laser,[33] basically in accord with our experimental values of 110.6 and 183.5 cm^{-1} respectively under the 532 nm laser shown in Figure 3d and S6, in which there is an obvious red shift for A_{1g} with the reduce of the layer number but no change for E_g, compared to the change of Raman spectra of MoS_2 (blue and red shifts for E_{2g} and A_{1g} with reducing the layer number).[34] Moreover, the Raman map of the blue line region of the optical microscopy image displays the monolayer $SnSe_2$ is easily identified from different layer sample, shown in Figure 3b. The A_{1g} mode shows low intensity in monolayer but is still detectable and can be clearly distinguished from bulk to monolayer $SnSe_2$.(Figure 3d) A plot of the intensity ratio of I(Si) and I($SnSe_2$) for the A_{1g} and E_g modes respectively with the function of the number of the layers is shown in Figure 3e. For the A_{1g} mode, the I(Si)/ I($SnSe_2$) intensity ratio of monolayer and bilayer are basically the same, and then decreases approximately linearly with the thickness. But for the E_g mode, the I(Si)/I($SnSe_2$) intensity ratio always decreases approximately linearly with increasing the thickness. Therefore, the variation of the I(Si)/ I($SnSe_2$) intensity ratio is basically normal.

2.3. Theoretical Calculations

The electronic band structures of bulk (Figure 4b), 4L (Figure S7b), 3L (Figure S7a), 2L (Figure 4c) and 1L (Figure 4d) have been obtained by the first principle calculation based on density functional theory (DFT) respectively. Figure 4b shows bulk $SnSe_2$ are a semiconductor with an indirect band gap of 0.710 eV, which is lower than the experimental value of 1.0 eV due to the insufficient cancellation of the self-interaction error by the approximate GGA functionals.[35] Of particular interest of our finding from the band structure is that the band gap is insensitive on the number of layers compared with the observations in MoS_2 and black phosphorus.[18], [36] In addition, the calculated results show $SnSe_2$ from bulk to monolayer always have the indirect band gaps, which have been confirmed by the photoluminescent measurement with no PL phenomenon from bulk to monolayer, which is different from MoS_2 which has an indirect bandgap for bulk but direct band gap for monolayer.[18]

2.4. The electronic properties of bilayered $SnSe_2$ FET

The electrical contacts made of Ti/Au films have been deposited by an e-beam evaporator after photolithography, shown in Figure 5a. The substrate and the electrode are attached to chip carrier fixtures for electrical testing. The current–voltage (I_d–V_d) curve and the transfer characteristics (I_d–V_g) of the fabricated $SnSe_2$ transistor in the absence of laser irradiation is shown in Figure 5b and 5c. It can be depicted that the bilayer $SnSe_2$ FET exhibited n-type

semiconducting behavior, which is consistent with theoretical results and previous literatures.[29] On the other hand, we also observe a clear hysteresis loop in the electrical characteristics, resulting from surrounding conditions or the charge transfer from neighboring adsorbates or trapping states on the substrate.[37] The mobility of the carriers can be calculated by $\mu = \frac{L}{W \times (\varepsilon_0 \varepsilon_r / d)} \times \frac{dI_{ds}}{dV_G} \times \frac{1}{V_{ds}}$, where L, W and d denote the channel length, width and the thickness of SiO_2 layer (285 nm in our devices), respectively. V_{ds}, I_{ds} and V_b denote the source–drain bias, current, and bottom gate voltage in the linear region in the I_d–V_g curve. ε_0 and ε_r are the vacuum dielectric constant and the dielectric constant of SiO_2 (ε_r = 3.9), respectively. The calculated mobility of our device is about 4 $cm^2 V^{-1} s^{-1}$, which is at least one order higher than that of other similar compounds such as GaS, GaSe, GaTe and WS_2,[16], [38] even though it is much lower than these of MoS_2 and WSe_2.[39], [40] Furthermore, the mobility can be improved by optimizing crystal quality, contact resistance and the dielectric environment similar to MoS_2 transistors, the mobility of which is increased from 0.1 $cm^2 V^{-1}s^{-1}$ to nearly 200 $cm^2V^{-1}s^{-1}$ by employing high-*k* gating of HfO_2 layer.[41] The relatively high mobility of the $SnSe_2$ transistor could be applied in optoelectronic and photonic applications. Figures 5c and 5d display the on/off ratio of FET fabricated by bilayer $SnSe_2$ is up to 10^3, compared with single digit ratio reported 84 nm-thick SnSe2 based FET[29] In the dark state, our device shows a typical behavior of n-type transistor and a threshold voltage of V_t = 5 V. When we illuminated the biased device using a focused 633 nm laser, the dark current increased in the range of 10 nA. As a result, the photocurrent dominates over the tunneling currents and thermionic currents in the operating working range, indicating that the $SnSe_2$ FET is suitable for photodetector device.

2.5. The optoelectronic properties of bilayered $SnSe_2$ photodetector

We probed the bilayer $SnSe_2$ FET devices (Figure 6a and 6b) and their time-dependent photoresponse to laser excitation using a focused laser beam (λ = 633 nm) and an illumination power of 4 mW. A parabolic mirror and micromechanical stage were used to localize the device. The spot size has a typical diameter of ~0.5 mm, resulting in an estimated maximum illumination intensity of ~ 0.64 W/cm^2. The time-dependent photocurrent measurement results are shown in Figure 6c and 6d. The photocurrent I_{ph} (I_{ph} = $I_{illuminated}$ - I_{dark}) of $SnSe_2$ FET is about 10^5 nA corresponding to a photoresponsivity of ~ 0.5 A/W under a source–drain bias of 100 mV. The photocurrent can be further increased by applying a higher source–drain voltage, as shown in Figure 6d. The decay time can be fitted by the following equation:

$I_{rise} = I_0 - A\exp(-(t-t_1)/\tau_1)$ and $I_{decay} = I_0 + B\exp(-(t-t_2)/\tau_2)$,[42] where τ is the time constant and t is the time when laser is switched on or off. Idark is the dark current, and A is the scaling constant. The fitted characteristic photoresponse time coefficients, τ_1 and τ_2, are 2.2 ± 0.3 ms (rise) and 3.2 ± 0.2 ms (fall), respectively, which is one of the fastest response times among all types of 2D photodetectors, e.g., 600 ms for 1L MoS_2,[43] 5.3 ms for few layered WS_2,[44] 6 ms for multilayer GaTe,[16] 20 ms for multilayer GaSe,[45] etc. On the other hand, the rise time and fall time can also be calculated by the time period between the 10% and 90% of the current in the arising and falling curves, as shown in Figure 6c. The rise time (τ1 = 2.1 ms) and fall time (τ_2 = 3.2 ms) are consistent with the former fitted values. Further improvement of the mobility by dielectric engineering or decreasing the thickness of the $SnSe_2$ layer may further boost the response time. More importantly, due to the phase changing property of $SnSe_2$, the performance of the $SnSe_2$ photodetector can be improved by phase engineering analogous to MoS_2.[46]

On the other hand, with the increasing of laser power, the photoresponse can be expressed by a power law $I_{PC} = CP^{\gamma}$ (C is a constant and P is the illumination power) as shown in Figure 6e. For the laser with the wavelength of 532 nm and 633 nm, γ is 0.90 and 0.82, respectively, indicating that the recombination kinetics of photocarriers involves both traps states and interactions between photogenerated carriers. The decrease of the photocurrent with the incident laser power can be attributed to the reduction of the numbers of photogenerated carriers available for extraction under high photon flux due to the Auger process or the saturation of recombination/trap states that influence the lifetime of the generated carriers.[47],[48] The Schottky junction formed at the metal–SnS_2 interfaces is also important to the photocurrent generation, which can be inferred from Figure 6f that a nonlinear effect is observed in the photocurrent generation with various bias voltage. Considering the trade-off between response time and responsivity for typical materials used in photodetectors, our $SnSe_2$ based photodetector shows a relatively faster response time compared to other two-dimensional metal chalcogenides, but slower than that of graphene photodetector which has an ultrahigh mobility. The responsivity of $SnSe_2$ based photodetector is higher than these of graphene,[49] WS_2[44] and WSe_2,[50] but still lower than these of MoS_2[43], [51] and GaTe,[16] which might be attributed to the lower light absorption efficiency and higher carriers scattering in $SnSe_2$ in the semiconductor channel.

3. Conclusion

The properties of few-layer and monolayer $SnSe_2$, a new 2D material whose components are both cheap and earth-abundant, have been firstly investigated systematically in this paper

using comprehensive characterization, device fabrication and measurement of electronic and optoelectronic device. We unambiguously identify monolayer and few-layer $SnSe_2$ by optical and atomic force microscope, whose monolayer thickness is ~0.87 nm. Moreover, combined with atomic force microscope, Raman spectra of monolayer and few-layer $SnSe_2$ have been studied, which show an obvious red shift for A_{1g} with the reduce of the layer number but no change for E_g. Electronic structure calculations indicate the bandgap is indirect from bulk to monolayer, consistent with the behavior observed in SnS_2 and contrast with MoS_2. We have successfully fabricated back-gated electronic and optoelectronic device based on bilayer $SnSe_2$ with thermal evaporated SiO_2 as dielectric layer, which exhibit a mobility up to 4 $cm^2V^{-1}s^{-1}$ and on/off ratio of 10^3 at room temperature and the dark state. Moreover, the bilayer SnSe2 photodetector upon illumination of 633 nm laser displays a good responsivity of 0.5 AW^{-1} and a very fast time response of 2.2 ± 0.3 ms (rise) and 3.2 ± 0.2 ms (fall), which make it also a promising 2D material for photodetection in the visible region.

4. Experimental Section

Synthesis and mechanical exfoliation of of $SnSe_2$ single crystals: Polycrystalline $SnSe_2$ was prepared by melting stoichiometric amounts of Sn powder (99.99 %, Sigma-Aldrich) and Se powder (99.995 %, Sigma-Aldrich), which were sealed in an evacuated quartz ampoule under vacuum at 10^{-6} Torr and then placed in one-zone tube furnace with the heating procedure: heated to 600 °C in 10 h, dwelt for 24 h, then naturally cooled to room temperature. The obtained sample, which is in the form of a shining polycrystalline mass, is the pure phase of $SnSe_2$ confirmed by powder X-ray diffraction (Figure S2). In order to obtain the high quality single crystals of $SnSe_2$, a direct transport method without the transport gas is applied due to the good volatility of $SnSe_2$ in vacuum. Prior to the growth of the single crystals, the $SnSe_2$ polycrystalline sample is grinded to the powder in a mortar and then sealed in a 23 cm-long quartz tube under vacuum 10^{-6} Torr. The quartz tube is placed in a two-zone furnace with the reaction zone at higher temperature 800 °C and the growth zone at a lower temperature 620 °C for three days. In this method, the shining black opaque single crystals of $SnSe_2$ is obtained in the growth zone (Figure 1c). Monolayer and few-layer $SnSe_2$ flakes were mechanically exfoliated from bulk $SnSe_2$ single crystals and transferred to a silicon substrate

with a 285 nm thick silica layer using the scotch tape-based mechanical exfoliation method, which was widely employed for preparation of monolayer graphene and transitional metal dichalcogenides (TMD).

Elemental Analysis: Semi-quantitative microprobe analyses on the single crystals of $SnSe_2$ were performed with the aid of a field emission scanning electron microscope (JSM-5410) equipped with an energy dispersive X-ray spectroscope (EDX, Oxford INCA). The energy dispersive spectra (EDS) taken on visibly clean surfaces of the sample proved the presence of Sn and Se with the formula $SnSe_{1.96(2)}$ shown in Figure 1d.

Powder X-ray Diffraction: The powder XRD patterns were collected using a Rigaku DMAX 2500 diffractometer with monochromatized Cu-Kα radiation at room temperature in the 2θ range of 10–85° with a scan step width of 0.05°. The measured X-ray powder diffraction patterns were in accordance with the calculated ones simulated from the single crystal data as shown in Figure S1.

TEM sample preparations and AD-STEM imaging and image simulations: The TEM sample was prepared by transferring the $SnSe_2$ flakes onto lacey-carbon grid after evaporating a drop of IPA solvent and etching away the underneath SiO_2 layer with potassium hydroxide solution. The as-prepared TEM membranes were briefly irradiated in TEM mode before ADF-STEM characterization. The ADF-STEM were done with a FEI Titan ChemiSTEM equipped with a probe corrector. This microscope was operated with an acceleration voltage of 80 kV. The convergent angle for illumination is about 22 mrad with a probe current of 70 pA, and the collection angle is about 43.4 to 200 mrad. ADF-STEM image simulations of pristine SnSe2 were done with software STEMSIM.51 The input parameters were set according to the experiment conditions: collection angle is about 45 to 200 mrad, acceleration voltage and C3 is 80 kV and 1.5 µm respectively. A Wiener and average background subtracted filter is applied to Figure 2a and 2d, based on R. Kilaas's work and developed by David Mitchell.

Thickness measurements: The thickness measurements of monolayer and few-layer were carried out in atomic force microscopy (DI-3100), which shows the thickness of monolayer $SnSe_2$ is 0.87 nm shown in Figure 3c.

Raman spectra: Analysis of atomically thin $SnSe_2$ flakes and bulk sample by Raman spectroscopy was carried out on a WITec CRM200 confocal Raman microscopy system with the excitation line of 532 nm and an air-cooling charge-coupled device (CCD) as the detector (WITec Instruments Corp, Germany).

Calculations of band structure of $SnSe_2$ from bulk to monolayer: The first-principles calculations are based on the generalized gradient approximation (GGA)[53] using the projector augmented wave method[54], [55] as implemented in the VASP package.[56], [57] The kinetic energy cutoff of 500 eV was used, and the spin-orbit coupling was included in all the calculations. A vacuum layer of 15 Å was adopted to avoid interactions between neighboring layers for slab calculations. The numerical integration of the Brillouin zone was performed based on a 8 × 8 × 6 k-point mesh-grid for 3D bulk $SnSe_2$ and a 8 × 8 × 1 k-point mesh-grid for 2D $SnSe_2$.

The fabrication and measurements of the devices: The devices were fabricated by standard optical lithography and deposited Ti/Au (20 nm/80 nm) as contact electrodes using electron-beam evaporation. The final devices were annealed at 400 K for 2 h with the protection of nitrogen in order to remove resist residues and enhance the metallic contacts. Electrical characterization was performed by current–voltage measurements on a probe station using a semiconductor characterizqation system (Agilent, B1500A). Forthermore, the phototransistor performance were measured using a 633 nm laser.

Supporting Information

Supporting Information is available from the Wiley Online Library or from the author.

Acknowledgements

This work was supported by the National Research Foundation Singapore under NRF RF Award No. NRF-RF2013-08. This work as also supported by MOE2011-T2-2-147 and MOE2011-T3-1-005 from Ministry of Education, Singapore. Part of the electron microscopy characterizations were carried out at the Center for Electron Microscopy of Zhejiang University. W.L. and C.J. acknowledged financial support by the National Basic Research Program of China (2014CB932500 and 2015CB921000), the National Science Foundation of China (51222202, 51410305074 and 51472215), the Program for Innovative Research Team in University of Ministry of Education of China (IRT13037) and the Fundamental Research Funds for the Central Universities (2014XZZX003-07)

[1] K. S. Novoselov, A. K. Geim, S. V. Morozov, D. Jiang, Y. Zhang, S. V. Dubonos, I. V. Grigorieva, A. A. Firsov. *Science* **2004,** *306*, 666.

[2] Y. B. Zhang, Y. W. Tan, H. L. Stormer, P. Kim. *Nature* **2005,** *438*, 201.

[3] K. S. Novoselov, A. K. Geim, S. V. Morozov, D. Jiang, M. I. Katsnelson, I. V. Grigorieva, S. V. Dubonos, A. A. Firsov. *Nature* **2005,** *438*, 197.

[4] A.Rycerz, J. Tworzydlo, C. W. J. Beenakker. *Nat. Phys.* **2007,** *3*, 172.

[5] M. Corso, W. Auwarter, M. Muntwiler, A. Tamai, T. Greber, J. Osterwalder. *Science* **2004,** *303*, 217.

[6] L. Song, L. J. Ci, H. Lu, P. B. Sorokin, C. H. Jin, J. Ni, A. G. Kvashnin, D. G. Kvashnin, J. Lou, B. I. Yakobson, P. M. Ajayan. *Nano Lett.* **2010,** *10*, 3209.

[7] Z. Liu, L. L. Ma, G. Shi, W. Zhou, Y. J. Gong, S. D. Lei, X. B. Yang, J. N. Zhang, J. J. Yu, K. P. Hackenberg, A. Babakhani, J. C. Idrobo, R. Vajtai, J. Lou, P. M. Ajayan. *Nat. Nanotechnol.* **2013,** *8*, 119.

[8] E. Rokuta, Y. Hasegawa, K. Suzuki, Y. Gamou, C. Oshima, A. Nagashima. *Phys. Rev. Lett.* **1997,** *79*, 4609.

[9] S. Najmaei, Z. Liu, W. Zhou, X. L. Zou, G. Shi, S. D. Lei, B. I. Yakobson, J. C. Idrobo, P. M. Ajayan, J. Lou. *Nat. Mater.* **2013,** *12*, 754.

[10] K. F. Mak, K. L. He, J. Shan, T. F. Heinz. *Nat. Nanotechnol.* **2012,** *7*, 494.

[11] Q. Q. Ji, Y. F. Zhang, T. Gao, Y. Zhang, D. L. Ma, M. X. Liu, Y. B. Chen, X. F. Qiao, P. H. Tan, M. Kan, J. Feng, Q. Sun, Z. F. Liu. *Nano Lett.* **2013,** *13*, 3870.

[12] Y. Zhang, T. R. Chang, B. Zhou, Y. T. Cui, H. Yan, Z. K. Liu, F. Schmitt, J. Lee, R. Moore, Y. L. Chen, H. Lin, H. T. Jeng, S. K. Mo, Z. Hussain, A. Bansil, Z. X. Shen. *Nat. Nanotechnol.* **2014,** *9*, 111.

[13] X. Lu, M. I. B. Utama, J. H. Lin, X. Gong, J. Zhang, Y. Y. Zhao, S. T. Pantelides, J. X. Wang, Z. L. Dong, Z. Liu, W. Zhou, Q. H. Xiong. *Nano Lett.* **2014,** *14*, 2419.

[14] Y. F. Lin, Y. Xu, S. T. Wang, S. L. Li, M. Yamamoto, A. Aparecido-Ferreira, W. W. Li, H. B. Sun, S. Nakaharai, W. B. Jian, K. Ueno, K. Tsukagoshi. *Adv. Mater.* **2014,** *26*, 3263.

[15] Liu, W.; Kang, J. H.; Sarkar, D.; Khatami, Y.; Jena, D.; Banerjee, K. *Nano Lett.* **2013,** *13*, 1983-1990.

[16] F. C. Liu, H. Shimotani, H. Shang, T. Kanagasekaran, V. Zolyomi, N. Drummond, V. I. Fal'ko, K. Tanigaki. *ACS Nano* **2014,** *8*, 752.

[17] S. R.Tamalampudi, Y. Y. Lu, U. R. Kumar, R. Sankar, C. D. Liao, B. K. Moorthy, C. H. Cheng, F. C. Chou, Y. T. Chen. *Nano Lett.* **2014,** *14*, 2800.

[18] L. K. Li, Y. J. Yu, G. J. Ye, Q. Q. Ge, X. D. Ou, H. Wu, D. L. Feng, X. H. Chen, Y. B. Zhang. *Nat. Nanotechnol*. **2014,** *9*, 372.

[19] M.Chhowalla, G. A. J. Amaratunga. *Nature* **2000,** *407*, 164.

[20] J.Xiao, D. W. Choi, L. Cosimbescu, P. Koech, J. Liu, J. P. Lemmon. *Chem. Mater.* **2010,** *22*, 4522.

[21] Y. G. Li, H. L. Wang, L. M. Xie, Y. Y. Liang, G. S. Hong, H. J. Dai. *J. Am. Chem. Soc.* **2011,** *133*, 7296.

[22] Q. H. Wang, K. Kalantar-Zadeh, A. Kis, J. N. Coleman, M. S. Strano. *Nat. Nanotechnol.* **2012,** *7*, 699.

[23] V. Podzorov, M. E. Gershenson, C. Kloc, R. Zeis, E. Bucher. *Appl. Phys. Lett.* **2004,** *84*, 3301.

[24] T. Tani, T. Osada, S. Tanaka. *Solid State Commun.* **1977,** *22*, 269.

[25] J. A. Galvis, L. Chirolli, I. Guillamon, S. Vieira, E. Navarro-Moratalla, E. Coronado, H. Suderow, F. Guinea. *Phys. Rev. B* **2014,** *89*.

[26] A. D. Yoffe. *Chem. Soc. Rev.* **1976,** *5*, 51-78.

[27] D. Voiry, H. Yamaguchi, J. W. Li, R. Silva, D. C. B. Alves, T. Fujita, M. W. Chen, T. Asefa, V. B. Shenoy, G. Eda, M. Chhowalla. *Nat. Mater.* **2013,** *12*, 850.

[28] B. Mahler, V. Hoepfner, K. Liao, G. A. Ozin. *J. Am. Chem. Soc.* **2014,** *136*, 14121.

[29] Y. Su, M. A. Ebrish, E. J. Olson, S. J. Koester. *Appl. Phys. Lett.* **2013,** *103*.

[30] R. Y. Wang, M. A. Caldwell, R. G. D. Jeyasingh, S. Aloni, R. M. Shelby, H. S. P. Wong, D. J. Milliron. *J. Appl. Phys.* **2011,** *109*.

[31] T. S. Pan, D. De, J. Manongdo, A. M. Guloy, V. G. Hadjiev, Y. Lin, H. B. Peng. *Appl. Phys. Lett.* **2013,** *103*.

[32] Y. Huang, E. Sutter, J. T. Sadowski, M. Cotlet, O. L. A. Monti, D. A. Racke, M. R. Neupane, D. Wickramaratne, R. K. Lake, B. A. Parkinson, P. Sutter. *ACS Nano* **2014,** *8*, 10743.

[33] D. G. Mead, J. C. Irwin. *Solid State Commun.* **1976,** *20*, 885.

[34] H. Li, Q. Zhang, C. C. R. Yap, B. K. Tay, T. H. T. Edwin, A. Olivier, D. Baillargeat. *Adv. Funct. Mater.* **2012,** *22*, 1385.

[35] K. M. S. Etheredge, R. Mackay, G. L. Schimek, S. J. Hwu. *Inorg. Chem.* **1996,** *35*, 7919.

[36] K. F. Mak, C. Lee, J. Hone, J. Shan, T. F. Heinz. *Phys. Rev. Lett.* **2010,** *105*.

[37] H. M. Wang, Y. H. Wu, C. X. Cong, J. Zh. Shang, T. Yu. *ACS Nano* **2010,** *4*, 7221.

[38] D. J. Late, B. Liu, J. J. Luo, A. M. Yan, H. S. S. R. Matte, M. Grayson, C. N. R. Rao, V. P. Dravid. *Adv. Mater.* **2012,** *24*, 3549.

[39] X. Cui, G. H. Lee, Y. D. Kim, G. Arefe, P. Y. Huang, C. H. Lee, D. A. Chenet, X. Zhang, L. Wang, F. Ye, F. Pizzocchero, B. S. Jessen, K. Watanabe, T. Taniguchi, D. A. Muller, T. Low, P. Kim, J. Hone. *Nat. Nanotechnol.* **2015,** *10*, 534.

[40] H. J. Chuang, X. B. Tan, N. J. Ghimire, M. M. Perera, B. Chamlagain, M. M. C. Cheng, J. Q. Yan, D. Mandrus, D. Tomanek, Z. X. Zhou. *Nano Lett.* **2014,** *14*, 3594.

[41] B. Radisavljevic, A. Radenovic, J. Brivio, V. Giacometti, A. Kis. *Nat. Nanotechnol.* **2011,** *6*, 147.

[42] B. Chitara, L. S. Panchakarla, S. B. Krupanidhi, C. N. R. Rao. *Adv. Mater.* **2011,** *23*, 5419.

[43] O. Lopez-Sanchez, D. Lembke, M. Kayci, A. Radenovic, A. Kis. *Nat. Nanotechnol.* **2013,** *8*, 497.

[44] N. Perea-Lopez, A. L. Elias, A. Berkdemir, A. Castro-Beltran, H. R. Gutierrez, S. M. Feng, R. T. Lv, T. Hayashi, F. Lopez-Urias, S. Ghosh, B. Muchharla, S. Talapatra, H. Terrones, M. Terrones. *Adv. Funct. Mater.* **2013,** *23*, 5511.

[45] P. A. Hu, Z. Z. Wen, L. F. Wang, P. H. Tan, K. Xiao. *ACS Nano* **2012,** *6*, 5988.

[46] R. Kappera, D. Voiry, S. E. Yalcin, B. Branch, G. Gupta, A. D. Mohite, M. Chhowalla. *Nat. Mater.* **2014,** *13*, 1128.

[47] Z. H. Sun, Z. K. Liu, J. H. Li, G. A. Tai, S. P. Lau, F. Yan. *Adv. Mater.* **2012,** *24*, 5878.

[48] G. Konstantatos, M. Badioli, L. Gaudreau, J. Osmond, M. Bernechea, F. P. G. de Arquer, F. Gatti, F. H. L. Koppens. *Nat. Nanotechnol.* **2012,** *7*, 363.

[49] M. C. Lemme, F. H. L. Koppens, A. L. Falk, M. S. Rudner, H. Park, L. S. Levitov, C. M. Marcus. *Nano Lett.* **2011,** *11*, 4134.

[50] D. J. Groenendijk, M. Buscema, G. A. Steele, S. M. de Vasconcellos, R. Bratschitsch, H. S. J. van der Zant, A. Castellanos-Gomez. *Nano Lett.* **2014,** *14*, 5846.

[51] Z. Y. Yin, H. Li, H. Li, L. Jiang, Y. M. Shi, Y. H. Sun, G. Lu, Q. Zhang, X. D. Chen, H. Zhang. *ACS Nano* **2012,** *6*, 74-80.

[52] A. Rosenauer, M. Schowalyer. STEMSIM—a new software tool for simulation of STEM HAADF Z-contrast imaging[M]//Microscopy of semiconducting materials 2007. Netherlands **2008,** 170.

[53] J. P. Perdew, K. Burke, M. Ernzerhof. *Phys. Rev. Lett.* **1996,** *77,* 3865.

[54] P. E. Blochl. *Phys. Rev. B* **1994,** *50,* 17953.

[55] G. Kresse, D. Joubert. *Phys. Rev. B* **1999,** *59,* 1758.

[56] G. Kresse, J. Hafner. *Phys. Rev. B* **1993,** *48,* 13115.

[57] G. Kresse, J. Furthmuller. *Phys. Rev. B* **1996,** *54,* 11169.

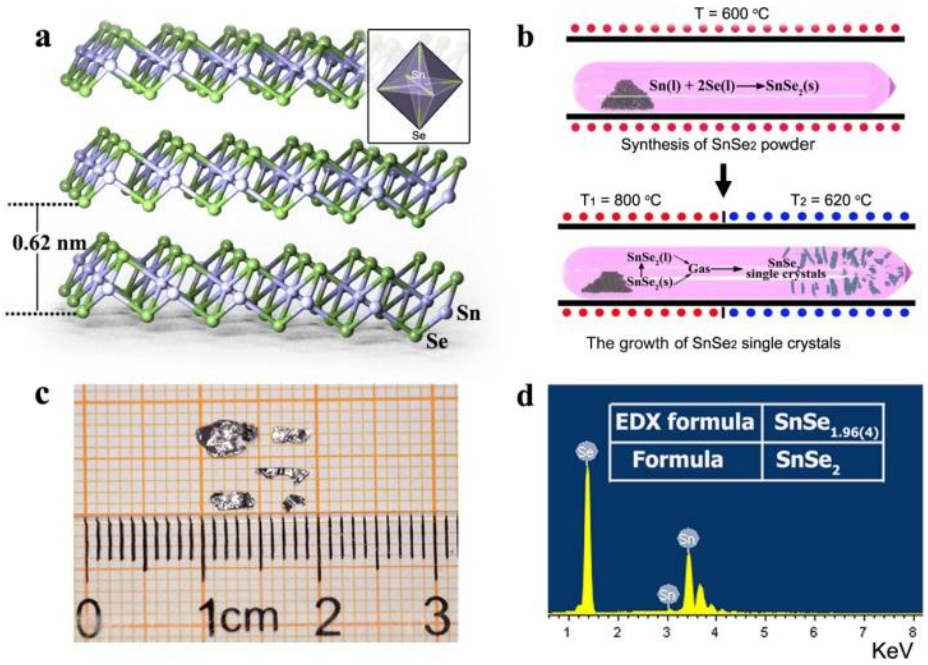

Figure 1. Synthesis and morphologies of $SnSe_2$ bulk single crystals. (a) The structure of $SnSe_2$ with 0.62 nm of the thickness of monolayer, inset: $SnSe_6$ octahedron. (b) The synthesis process of $SnSe_2$ polycrystalline powder (up) and the growth process of $SnSe_2$ single crystals using vaper mass transport (VMT) technique without transport gas (down). (c) The optical image of $SnSe_2$ single crystals with the size of several millimeters. (d) EDX result of $SnSe_2$ single crystal.

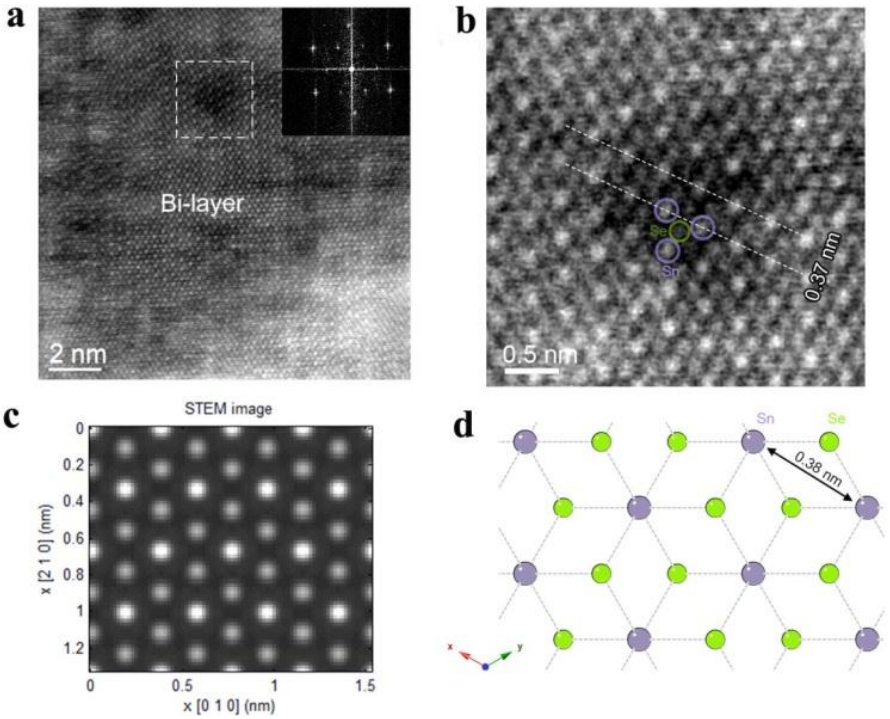

Figure 2. Atomically resolved imaging of few layered $SnSe_2$. (a) $SnSe_2$ film dominated by Bi-layered $SnSe_2$. A small area of monolayer $SnSe_2$ is highlighted by the white rectangle. Inset is the corresponding Fast Fourier Transform (FFT) pattern. (b) A close-up of the monolayer area. The Sn-Sn bond with 0.37 nm, which fits to the crystal model in (c) and (d) very well.

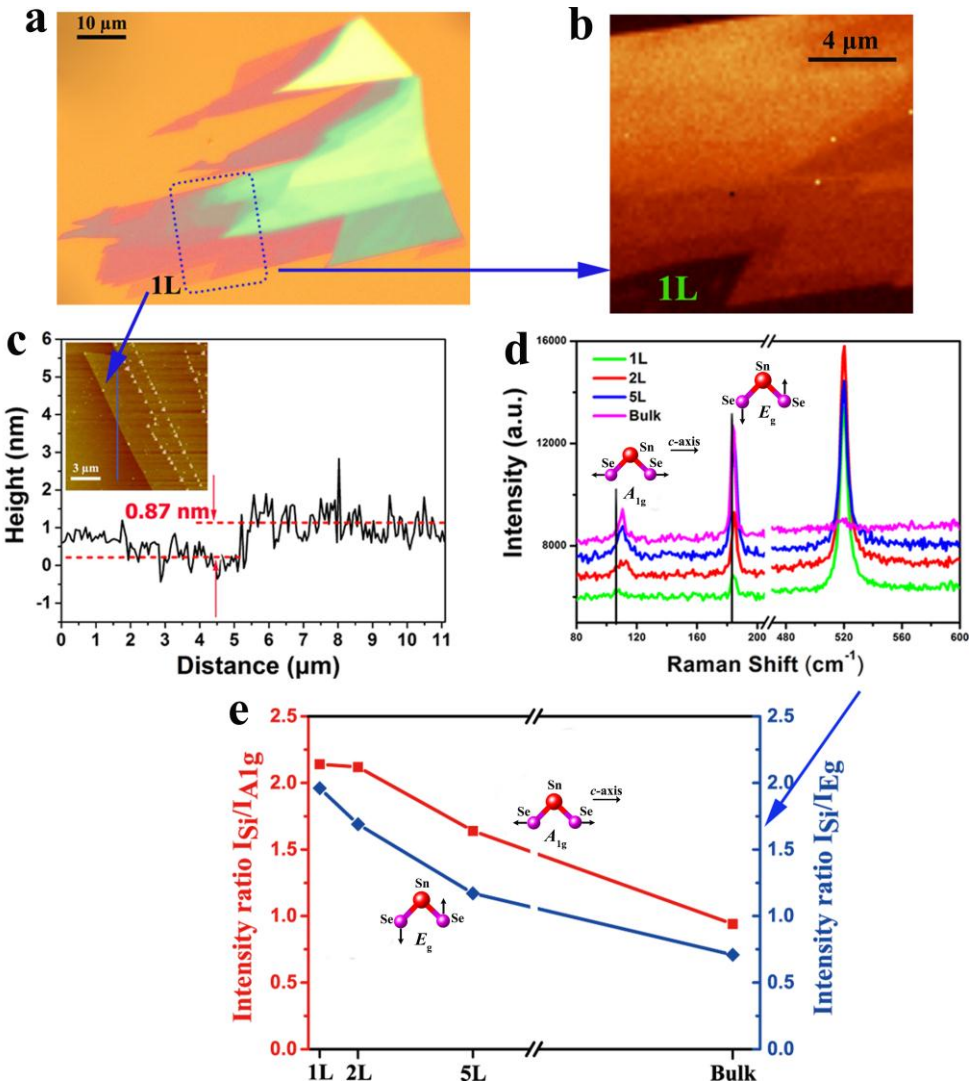

Figure 3. The characterization of few-layer and monolayer $SnSe_2$. (a) Optical image of $SnSe_2$ flake placed on the surface of a silicon wafer capped by 285-nm-thick silicon dioxide. (b) Raman mapping image of the blue region in (a), which clearly displays the monolayer. (c) The thickness of monolayer $SnSe_2$, inset: AFM image of the different thick sample. (d) Normalized Raman spectra of $SnSe_2$ from monolayer to bulk. The intensity of Si peak is set as constant. (e) The Raman intensity ratio of Si/A_{1g} and Si/E_g with the dependence of the various thick layers. The inset in Figure 3d and 3e is the schematics of displacement of atom for Raman active A_{1g} and E_g modes in $SnSe_2$.

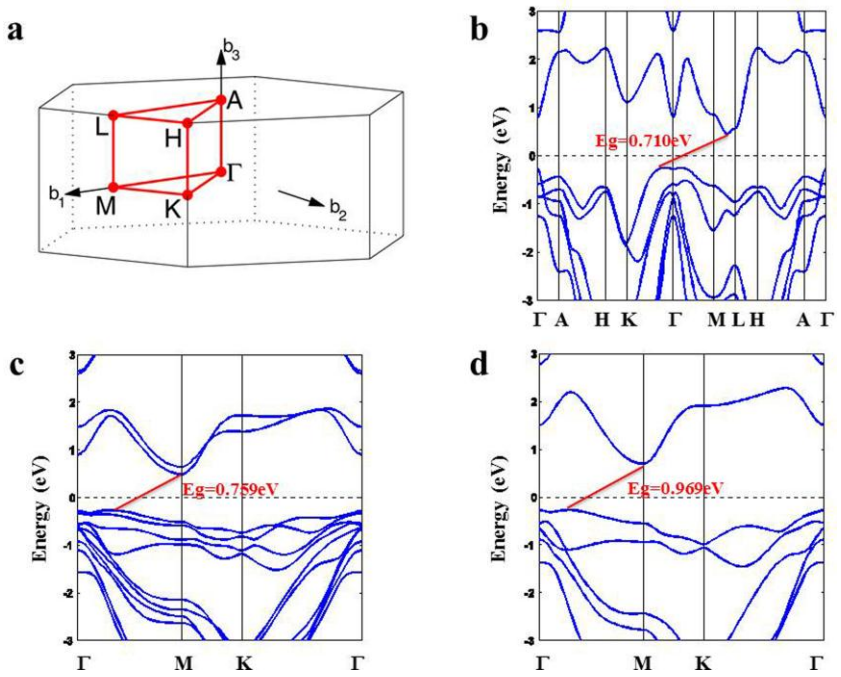

Figure 4. The calculated electronic band structures of $SnSe_2$ with the spin-orbit couple (SOC) from bulk to monolayer. (a) The Brillouin zone of $SnSe_2$. (b)–(d) The band structures of bulk (b), bilayer (c) and monolayer (d). The indirect band gaps of bulk and, bilayer, and monolayer $SnSe_2$ are 0.710, 0.759 and 0.969 eV, respectively.

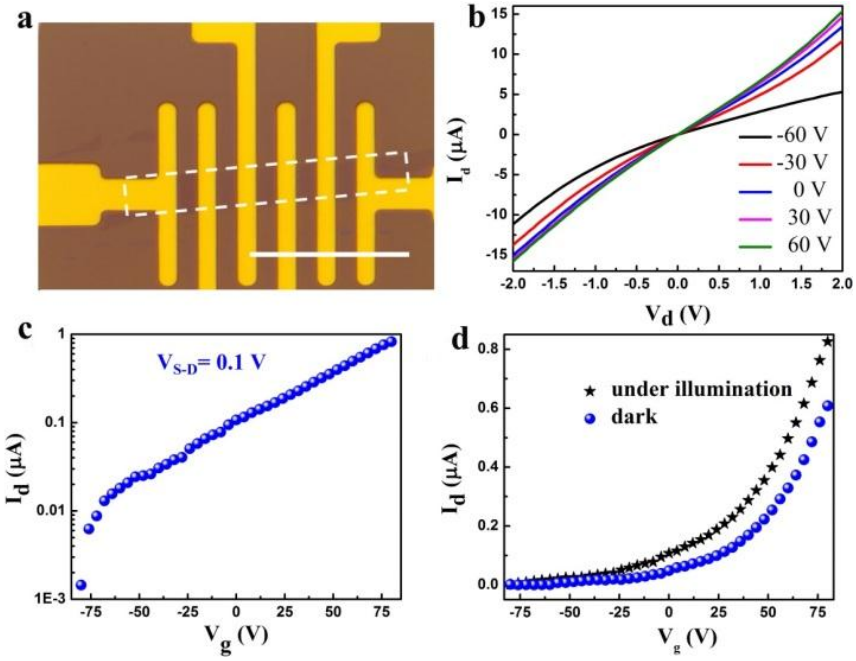

Figure 5. The electrical property of the fabricated $SnSe_2$ bilayer FET. (a) Optical microscopy image of a bilayer SnSe2 FET device with Ti/Au as the electrodes on Si/SiO_2 substrate. The scale bar is 20 μm. The white-color dashed line indicates the sample area. (b) Current–voltage (I_d–V_d) curve acquired with different gate voltages (without light illumination). (c) Gating response (I_d–V_g) of the $SnSe_2$ FET acquired for a backgate voltage V_g between -80 V and 80 V with a source–drain voltage ($V_{S–D}$) of 0.1 V (without light illumination). (d) Gating response (I_d–V_g) of the $SnSe_2$ transistor in dark and illuminated states. The illumination intensity is 500 W/cm^2.

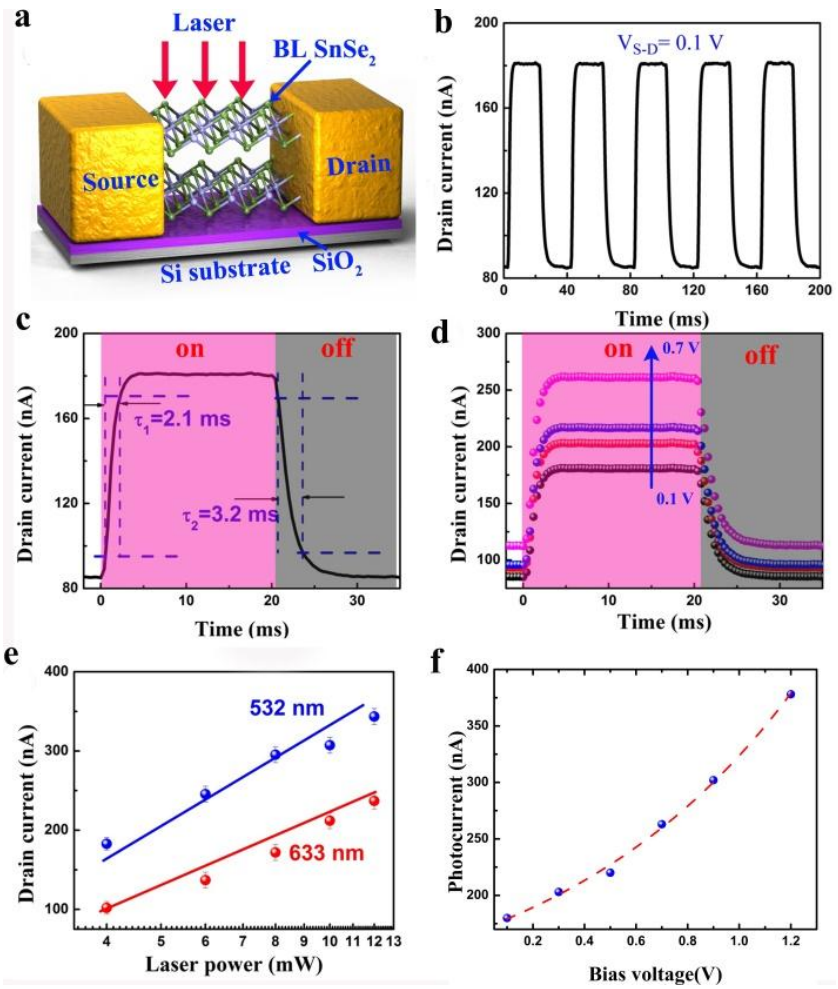

Figure 6. The optoelectronic properties of the fabricated $SnSe_2$ bilayer device. (a) Schematic representation of the photodetector device consisting of a bi-layered $SnSe_2$ on SiO_2/Si wafer with laser illumination. (b) Time-resolved photoresponse of the device recorded for a bias voltage of 0.1 V and zero gate voltage. (c) Photocurrent dynamics of one period of the time-resolved photoresponse. The laser used in Figure 6b and 6c is 633 nm laser with a power of 4 mW. (d) Time-resolved photoresponse of the device recorded for different source–drain voltages varying from 0.1 V to 0.7 V at a step of 0.2 V with 633 nm laser illumination (4 mW). (e) Power dependences of the photocurrent with 532 nm and 633 nm laser illumination recorded at V_{SD}=0.1 V. (f) Photocurrent response-bias characteristic of the device under 632 nm laser illumination with power of 4 mW.

ToC figure

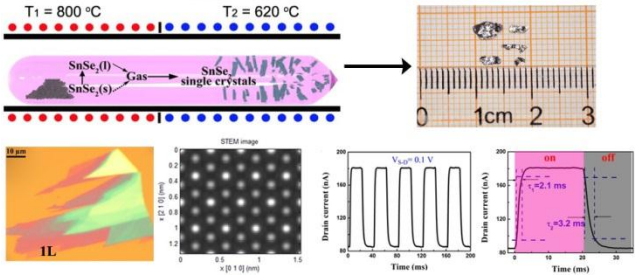
T1 = 800 °C
T2 = 620 °C
SnSe2(l)
SnSe2(s)
Gas
SnSe2 single crystals
0 1cm 2 3
1L
STEM image
Drain current (nA)
Time (ms)
on
off
τ1=2.1 ms
τ2=3.2 ms